Combustion and Flame 232 (2021) 111516

Contents lists available at ScienceDirect

Combustion and Flame

journal homepage: www.elsevier.com/locate/combustflame

# A comprehensive experimental and kinetic modeling study of 1-hexene

Shijun Dong[a,*], Christopher Aul[b], Claire Gregoire[c], Sean P. Cooper[c], Olivier Mathieu[c], Eric L. Petersen[c], Jose Rodriguez[d], Fabian Mauss[d], Scott W. Wagnon[e], Goutham Kukkadapu[e], William J. Pitz[e], Henry J. Curran[a]

[a] Combustion Chemistry Centre, School of Chemistry, Ryan Institute, MaREI, NUI Galway, Ireland
[b] Department of Physics, Engineering, and Astronomy, Stephen F. Austin State University, Nacogdoches, TX, USA
[c] J. Mike Walker '66 Department of Mechanical Engineering, Texas A&M University, College Station, TX, USA
[d] Thermodynamics and Thermal Process Engineering, Brandenburg University of Technology, Siemens-Halske-Ring 8, 03046 Cottbus, Germany
[e] Materials Science Division, Lawrence Livermore National Laboratory, Livermore, USA

ARTICLE INFO

*Article history:*
Received 18 January 2021
Revised 14 May 2021
Accepted 17 May 2021

*Keywords:*
1-hexene
Oxidation
Rapid compression machine
High-pressure shock tube
Ignition delay time

ABSTRACT

It is important to understand the low-temperature chemistry of 1-hexene as it is used as a representative alkene component in gasoline surrogate fuels. Ignition delay times (IDTs) of 1-hexene measured in rapid compression machines (RCMs) can be used to validate its low-temperature chemistry. However, volume history profiles are not available for published RCM IDT data. This has restricted the validation of the low-temperature chemistry of 1-hexene at engine-relevant conditions (i.e. at low temperatures and high pressures). Thus, new RCM IDT data with associated volume history profiles are needed. In this study, both an RCM and a high-pressure shock tube (ST) are employed to measure IDTs of 1-hexene at equivalence ratios of 0.5, 1.0 and 2.0 in 'air' and at pressures of 15 and 30 atm. A cool-flame (first stage) and total (second stage) ignition was observed in the RCM experiments. Moreover, carbon monoxide and water versus time histories produced during 1-hexene oxidation at highly diluted conditions were measured in a ST. A new detailed chemical kinetic model describing 1-hexene oxidation is proposed and validated using these new measured data together with various experimental data available in the literature. The kinetic model can predict well the auto-ignition behavior and oxidation processes of 1-hexene at various conditions. The rate constants and branching ratio for hydroxyl radical addition to the double bond of 1-hexene are particularly important and discussed based on the experimental and theoretically calculated results from previous studies as well as validation results from jet-stirred reactor (JSR) species profiles. Flux and sensitivity analyses are performed to determine the important reaction classes for 1-hexene oxidation and show that the reactions associated with hydroxy radical addition to the double bond contribute most to the low-temperature reactivity of 1-hexene. In the negative temperature coefficient (NTC) regime, the isomerization of hexenyl-peroxy radicals promotes fuel reactivity due to its associated chain branching pathways.



## 1. Introduction

1-Hexene is often used as a representative alkene component in gasoline surrogate fuels [1–7], and it is also an intermediate product of *n*-hexane oxidation. A number of studies have been performed to investigate the combustion chemistry of 1-hexene [8–11]. These studies were performed in various facilities, including shock tubes (STs) [9,12], rapid compression machines (RCMs) [10,12] and jet-stirred reactors (JSR) [11,13,14]. Yahyaoui et al. [9,14] studied the oxidation of 1-hexene in both a ST and in a JSR, and a kinetic model was proposed. Mehl et al. [10,12] investigated the auto-ignition behavior of 1-, 2- and 3-hexene in both an RCM and in a high-pressure shock tube (HPST), and a kinetic model was also developed to simulate these data. However, in simulating the RCM data to calibrate heat losses/facility effects, the same parameters were used in all of the simulations. This affects the prediction of experimental data with long ignition delay times (IDTs).

* Corresponding author.
*E-mail address:* shijun.dong@nuigalway.ie (S. Dong).

https://doi.org/10.1016/j.combustflame.2021.111516

Meng et al. [11] studied 1-hexene oxidation based on comprehensive species data measured in a JSR [13] and a new kinetic model was proposed. In their study, the model was also validated using the RCM data measured by Vanhove et al. [15] and Mehl et al. [10,12]. However, as there are no volume profiles available, the constant volume assumption was used in the simulations and this significantly affects the simulation results at low temperatures and prevents the validation of the 1-hexene model to the accuracy required for current chemical kinetic models. In the low-temperature range, 1-hexene shows a more pronounced NTC behavior and a higher fuel reactivity than 2-hexene or 3-hexene [10,12,15]. Since 1-hexene is an important gasoline surrogate, it is necessary to validate its low-temperature chemistry at engine relevant conditions (i.e. at low temperatures and high pressures). Thus, new IDT measurements in an RCM with effective volume history profiles are needed. Most of the literature ST data related to 1-hexene oxidation are limited to IDTs. Speciation measurements in the ST can provide multiple targets for kinetic model validation at high temperatures.

Moreover, most of the hexene mechanisms were proposed by different groups, and the chemistry controlling the low-temperature reactivity differs among them [8–11]. Therefore, a detailed understanding of alkene chemistry is less understood compared to alkanes. New quantum chemistry calculation results have been published over the years describing important reactions pertaining to alkene chemistry [16–25], and these results, used in detailed chemical kinetic models, can help understand and better predict alkene chemistry. In a previous study, we have used consistent rate constants to describe chemical kinetics in the low- to intermediate-temperature range for 1-alkene fuels [26]. The current study will focus on 1-hexene and further validate some important reaction pathways.

In this paper, IDTs of 1-hexene were measured using both an RCM and a HPST over a wide range of temperature (600 – 1300 K), at pressures of 15 and 30 atm. Moreover, for the first time, time histories of carbon monoxide and water produced during 1-hexene oxidation at highly diluted conditions and various equivalence ratios (0.5, 1.0, and 2.0) were measured in a ST at approximately 1.5 atm. A new kinetic model has been developed and validated against the new IDT data and species profiles measured in this study as well as the existing experimental data available in the literature.

## 2. Experimental specifications

### 2.1. Ignition delay time measurements

IDTs of 1-hexene were measured in both an RCM and in a HPST at NUI Galway, with a detailed description of these facilities provided previously [27,28]. The HPST has an internal diameter of 63.5 mm and a total length of 8.76 m, divided into three parts: a 5.73 m long driven section, a 3.0 m long driver section and a 3.0 cm long double-diaphragm section. In the HPST experiments, the incident shock velocity was determined using six pressure transducers (PCB, 113B24) installed in the sidewall, and another pressure transducer (Kistler 603C) installed in the endwall was used to determine the IDT. GasEq [29] was used to calculate the gas pressure and temperature behind the reflected shock wave, based on the incident shock velocity and initial mixture conditions. The RCM at NUI Galway has a twin-opposed piston configuration, which can achieve a fast compression time of approximately 16 ms. Creviced pistons are employed to improve post-compression temperature homogeneity in the reaction chamber. In the RCM experiments, the geometric compression ratio was fixed and the initial temperature was varied to achieve different compressed gas temperatures. These were calculated using GasEq [29] based on the measured compressed pressure and initial mixture conditions.

**Table 1**
Experimental conditions studied for1-hexene in the RCM and HPST.

| $T$ (K) | $p$ (atm) | $\varphi$ | dilution (%) |
|---|---|---|---|
| 600 – 1300 | 15, 30 | 0.5, 1.0, 2.0 | 75.5 – 78.1 |

The designed experiment conditions are given in Table 1. The mole fraction of dilution is determined using the total mole fraction of nitrogen and argon in the mixture. Both the RCM and HPST experiments were performed at air-like conditions, with the diluent (nitrogen or argon) and oxygen in a ratio of 79:21. In the RCM experiments, the initial temperature of the gas mixture was varied from room temperature to 150 °C. Moreover, for each test point of the RCM experiments, a non-reactive pressure trace, in which the $O_2$ content in the mixture is replaced by $N_2$, was also taken so that we can account for facility effects in our simulations.

As shown in Fig. 1, both the IDTs recorded in the HPST and RCM were determined using the measured pressure traces. Figure 1(b) shows the definitions of first-stage IDT and total IDT in the 1-hexene RCM experiments. The uncertainty in the IDT data from both facilities is ± 20%, as discussed previously [30].

High purity 1-hexene (> 98.5%) was provided by Sigma-Aldrich. High purity nitrogen (> 99%), oxygen (> 99%) and argon (> 99%), provided by BOC, were used in the experiments. The ST and RCM IDTs measured in this study are provided in Table S1 and S2 of the Supplementary material.

### 2.2. Carbon monoxide and water time-history measurements in a low-pressure shock tube

Carbon monoxide (CO) and water ($H_2O$) concentration vs time histories were measured using tunable IR lasers in two high-purity shock tubes at TAMU. The facilities and diagnostics were described in detail previously (see [31] and [32] for the CO shock tube and diagnostic and [33] for the $H_2O$ shock tube and diagnostic), and only a brief description of each shock tube and associated diagnostic is provided here. A thorough description of the procedures and considerations for these speciation measurements is available in Alturaifi et al. [34].

The two shock tubes used herein are made of stainless steel and employ a single diaphragm. The shock tube used to measure CO time histories has a 5.03 m long and 15.24 cm i.d. driven section (2.62 m length, 7.62 cm i.d. driver section). A quantum cascade laser (QCL) that produces light at 4566.17 nm was used for the CO measurements by accessing the R(12) line of the $1 \leftarrow 0$ band. The QCL was centered on the R(12) line using a removable cell (containing a low-pressure mixture of ~10% CO/Ar) prior to each experiment. Note that experiments were performed with and without He in the mixture. Adding helium is necessary to expedite vibrational relaxation in this type of mixture [32]. Tests with helium added show a 10% decrease in reflected-shock pressures compared to mixtures without helium at similar temperatures due to compressibility effects from the decreased molecular weight of the bath gas. There is little change in the induction delay time (see $\tau_{ind}$ below) and only a slight decrease in peak CO formation, around 5 – 7%, when compared to data without helium added at similar temperatures.

The primary data measured from the CO diagnostic were the species time history profiles but other measurements are extracted from the profiles that are used for mechanism validation. For the measurements of CO (equivalence ratios of $\varphi = 0.5$ and 1.0) the time at which the peak species mole fraction occurs ($\tau_{max}$) is recorded and compared with mechanism results. The time at

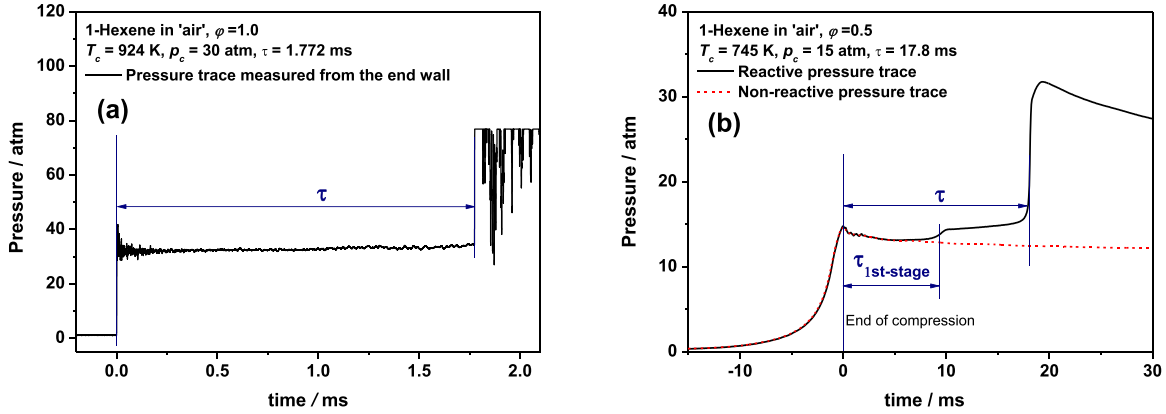


**Fig. 1.** Definitions of IDTs measured in (a) a HPST and (b) an RCM.

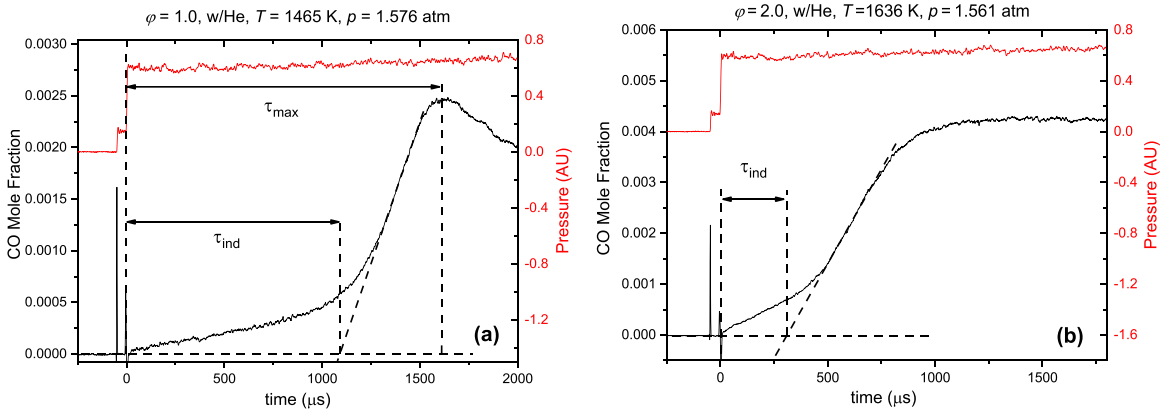


**Fig. 2.** Example CO profiles with definitions of $\tau_{max}$ and $\tau_{ind}$ for the (a) stoichiometric and fuel-lean ($\varphi = 0.5$) and (b) fuel-rich ($\varphi = 2.0$) mixtures tested.

which the beginning of the formation of CO is also recorded (induction time, $\tau_{ind}$) and is recorded for all mixtures where the CO diagnostic was utilized. The methods used to determine $\tau_{max}$ and $\tau_{ind}$ are illustrated in Fig. 2. The uncertainty in these measurements is essentially due to the uncertainty in the temperature (less than 1%). Given that the signals are easy to interpret due to their high signal-to-noise ratio, the uncertainty in the various delays measured herein is estimated to be approximately 10%.

The shock tube used to measure water has larger driven (6.78 m long, 16.2 cm i.d.) and driver (3.0 m, 7.62-cm i.d.) sections compared to that used to measure CO. The water time-history profiles were obtained using a tunable diode laser that accessed the $5_{5,1} \leftarrow 5_{5,0}$ transition in the $\nu_1 + \nu_3$ fundamental band by generating light at 1388.140 nm. A wavemeter (Burleigh WA-1000) was used to constantly monitor the wavelength of the laser. The laser path was enclosed and purged using $N_2$ to suppress laser beam attenuation by ambient water.

All mixtures (equivalence ratios of $\varphi = 0.5$, 1.0, and 2.0) were prepared manometrically in stainless-steel mixing tanks. Mixtures were highly diluted (99.5%) in inert gas (Ar or Ar/He). The large dilution level follows recent work with iso-octane [35] and allows for a limiting of the temperature rise induced by the exothermic reactions during the fuel oxidation while providing sufficient CO and $H_2O$ concentration for the measurements. Mixture compositions are given in Table S3 of the Supplementary material. The experiments were performed at pressures of ~1.5 atm in the temperature range of 1300 – 1900 K.

As detailed by Mathieu et al. [32] for CO and Mulvihill et al. [36] for $H_2O$, the uncertainty in the laser absorption measurements is a function of several parameters, such as broadband emission, uncertainty in the temperature and pressure behind the reflected shock wave, and line strength, among others. As such, the uncertainty varies between each test and as a function of time during each experiment (see Fig. 5 in [32] and Fig. 7 in [36]). However, to provide the reader with a visual estimation of the maximum uncertainty in the profiles, error bars are at the peak CO and $H_2O$ plateaus. In both cases, a very conservative uncertainty value is used, where the maximum values obtained in [32] for CO and in [36] for $H_2O$ are rounded to the superior figure (5% uncertainty for CO, and 6% for $H_2O$). Note that in the majority of the cases, the uncertainty is actually lower than represented herein.

## 3. Model development

This current model is developed based on a new base model, NUIGMech1.2, and the previous published mechanisms, *n*-hexane [37] and 1-hexene [38]. According to some new studies performed over the past decade or so [16–25], some new reaction classes were added and rate constants of the important reaction classes were updated [26]. THERM [39] integrated with updated group values from Burke et al. [40] and Li et al. [41] was used to calculate the thermochemical properties of the 1-hexene sub-mechanism species. Table 2 provides a summary of the important reaction classes updated with the corresponding references.

In this study, consistent rate constants and thermochemistry for low- to intermediate-temperature chemistry of 1-alkene fuels were used, and most of the updated reaction classes were discussed previously [26]. Thus, only the reaction pathways which are impor-

**Table 2**
Major updated reaction classes and references in the current model.

| No. | Reaction pathways | Reference |
|---|---|---|
| 1 | ȮH addition to $C = C$ double bond | [16] |
| 2 | Waddington mechanism, hydroxy–alkylperoxy radical isomerization and $H\dot{O}_2$ elimination | [19] |
| 3 | Alkenylperoxy radical isomerization and decomposition | [18,20] |
| 4 | 1-Hexene + $H\dot{O}_2$ | [17] |
| 5 | Isomerization and decomposition of hexenyl radicals | [23,24] |

**Table 3**
The structures of major species which relevant to 1-hexene oxidation.

| Species | Structure | Species | Structure |
|---|---|---|---|
| $C_6H_{12}$-1 |  | $\dot{C}_6H_{12}$OH-1J2 | 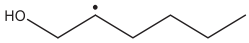 |
| $\dot{C}_6H_{11}$1-3 | 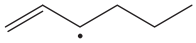 | $\dot{C}_6H_{12}$OH-2J1 | 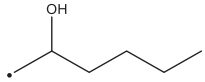 |
| $\dot{C}_6H_{11}$1-4 | 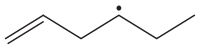 | $C_6H_{12}$OH-1$\dot{O}_2$-2 | 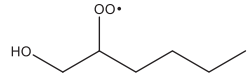 |
| $\dot{C}_6H_{11}$1-5 | 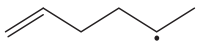 | $C_6H_{12}$OH-2$\dot{O}_2$-1 | 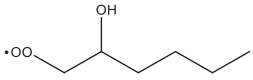 |
| $\dot{C}_6H_{11}$1-6 | 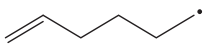 | $C_6H_{12}$OOH2-1Ȯ | 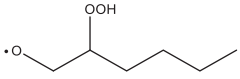 |
| $C_6H_{11}$1$\dot{O}_2$-3 | 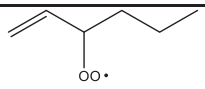 | $\dot{C}_6H_{11}$OH1Q2-4 | 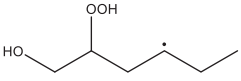 |
| $C_6H_{11}$1$\dot{O}_2$-4 | 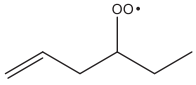 | $\dot{C}_6H_{11}$OH1Q2-5 | 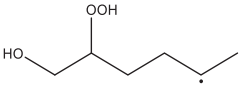 |
| $C_6H_{11}$1$\dot{O}_2$-5 | 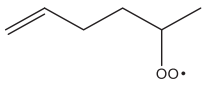 | $C_6H_{11}$OH1O2-5 | 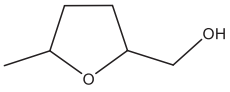 |
| $C_6H_{11}$1$\dot{O}_2$-6 | 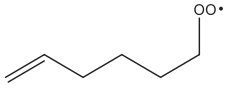 | $C_6H_{11}$OH1Q2-4$\dot{O}_2$ | 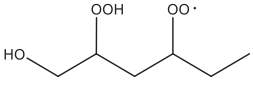 |
| $\dot{C}_6H_{10}$1OOH5-3 | 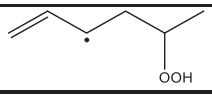 | $C_6H_{10}$OH1KET2-4 | 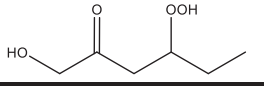 |

tant in 1-hexene chemistry are discussed in detail here. A list of the structures of the major species relevant to 1-hexene oxidation is provided in Table 3. The rate constants of the important reactions used in the current model are shown in Table 4. The final mechanism and species dictionary are available as Supplementary material.

Chemkin-PRO software [44] was used to simulate both the HPST and RCM the IDTs. Constant volume assumption was used in the simulations of the HPST data. The effective volume history profiles derived from the non-reactive ($O_2$ replaced with $N_2$) pressure traces were used in the RCM simulations to account for facility effects.

### 3.1. Hydroxy radical addition to the double bond

This is one of the most important reaction classes in the low-temperature oxidation of alkenes. The rate constants of this reaction from different studies [16,45,46] were compared in our previous study [26]. However, the employed rate constants and the branching ratio of ȮH radical addition to the terminal and central carbon of alkenes have not been well validated due to a lack of experimental data. Loison et al. [47] and Feltham et al. [48] experimentally studied this branching ratio at low temperatures, and they suggested a branching ratio of 50:50 for propene and this is consistent with the results from [16] and [45], while for 1-butene it was determined to be 75:25. ȮH radical addition to the double bond initiates the Waddington mechanism, with Eqns. 1 – 4 depicting it. In the low-temperature range, the Waddington mechanism is one of the major sources of aldehydes, which for 1-hexene are formaldehyde and *n*-pentanal. Therefore, different rate constants and branching ratios of ȮH radical addition to the terminal and central carbons will directly affect the fuel flux of the Waddington reaction pathways and hence affect the rates of formaldehyde and *n*-pentanal formation.

**Table 4**
Rate constants for the important reactions in the current model ($cm^3$/mol/s/cal units).

| No. | Reactions | *A* | *n* | $E_a$ | Reference |
|---|---|---|---|---|---|
| 1 | $C_6H_{12}$-1+ȮH<=>$\dot{C}_6H_{12}$OH-1J2 (DUP) | 2.872E+48 | −10.23 | 23,772. | [16] |
| 2 | $C_6H_{12}$-1+ȮH<=>$\dot{C}_6H_{12}$OH-1J2 (DUP) | 4.589E+32 | −6.310 | 6088. | [16] |
| 3 | $C_6H_{12}$-1+ȮH<=>$\dot{C}_6H_{12}$OH-2J1 (DUP) | 9.575E+47 | −10.23 | 23,772. | [16] |
| 4 | $C_6H_{12}$-1+ȮH<=>$\dot{C}_6H_{12}$OH-2J1 (DUP) | 1.530E+32 | −6.310 | 6088. | [16] |
| 5 | $\dot{C}_6H_{12}$OH-1J2+$O_2$<=>$C_6H_{12}$OH-1$\dot{O}_2$-2 | 3.487E+14 | −0.816 | −536.5 | [42] |
| 6 | $C_6H_{12}$OH-1$\dot{O}_2$-2<=>$C_6H_{12}$OOH2-1Ȯ | 2.610E+10 | +0.290 | 20,380. | [19] |
| 7 | $C_6H_{12}$OOH2-1Ȯ=>$PC_4H_9CHO$+$CH_2O$+ȮH | 2.118E+11 | +0.437 | 6184. | [25] |
| 8 | $C_6H_{12}$OH-1$\dot{O}_2$-2<=>$\dot{C}_6H_{11}$OH1Q2-4 | 7.150E+05 | +1.670 | 16,221. | [19] |
| 9 | $C_6H_{12}$OH-1$\dot{O}_2$-2<=>$\dot{C}_6H_{11}$OH1Q2-5 | 8.680E+02 | +2.310 | 13,600. | [19] |
| 10 | $C_6H_{12}$-1+ȮH<=>$\dot{C}_6H_{11}$1-3 + $H_2O$ | 1.212E+06 | +2.200 | −437.2 | [21] |
| 11 | $C_6H_{12}$-1+ȮH<=>$\dot{C}_6H_{11}$1-5 + $H_2O$ | 7.050E+09 | +0.935 | 504.7 | [43] |
| 12 | $C_6H_{12}$-1 + $O_2$<=>$\dot{C}_6H_{11}$1-3 + $H\dot{O}_2$ | 6.060E+01 | +3.450 | 34,600. | [22] |
| 13 | $C_6H_{12}$-1 + $H\dot{O}_2$<=>$\dot{C}_6H_{11}$1-3 + $H_2O_2$ | 7.820E−01 | +3.970 | 11,700. | [17] |
| 14 | $\dot{C}_6H_{11}$1-3 + $O_2$<=>$C_6H_{11}\dot{O}_2$-3 | 9.140E+02 | +2.179 | −2200. | [18] |
| 15 | $\dot{C}_6H_{11}$1-5 + $O_2$<=>$C_6H_{11}\dot{O}_2$-5 | 3.490E+14 | −0.816 | −537. | [42] |
| 16 | $C_6H_{11}\dot{O}_2$-3<=>$\dot{C}_6H_{10}$1OOH3-5 | 0.580E+03 | +2.245 | 15,500. | [18] |
| 17 | $C_6H_{11}\dot{O}_2$-5<=>$\dot{C}_6H_{10}$1OOH5-3 | 1.300E−05 | +4.830 | 9710. | [20] |
| 18 | $\dot{C}_6H_{11}$1-6<=>$\dot{C}_6H_{11}$1-3 | 4.220E+04 | +1.930 | 13,500. | [23] |
| 19 | $C_6H_{12}$-1 + $H\dot{O}_2$<=>$\dot{C}_6H_{12}$OOH1-2 | 2.820E+04 | +2.490 | 14,730. | [17] |
| 20 | $C_6H_{12}$-1 + $H\dot{O}_2$<=>$\dot{C}_6H_{12}$OOH2-1 | 1.360E+02 | +3.000 | 12,480. | [17] |

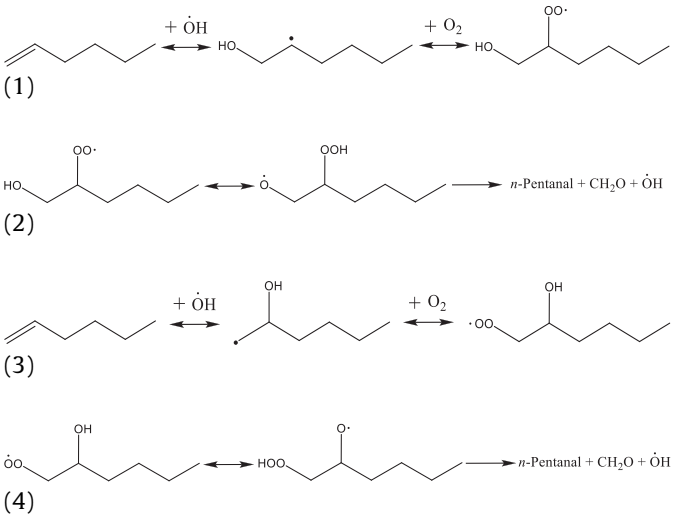


In this study, the comprehensive JSR data measured by Battin-Leclerc [13] and Meng et al. [11] were used to validate the current model for the branching ratio of ȮH addition. The predictions of formaldehyde, *n*-pentanal, hydroxyl cyclic ethers and other important species formed in the low-temperature chemistry are illustrated to discuss the employed rate constants and the branching ratio of ȮH addition. Flux analyses at 625 K and 850 K were performed and the results are provided in Fig. S1 of the Supplementary material. The results show that formaldehyde ($CH_2O$), *n*-pentanal ($pC_4H_9CHO$) and 2-methyl,5-hydroxymethyl-tetrahydrofuran ($C_6H_{11}$OH1O2–5) are the major species formed at low temperatures (600 – 700 K). The model results for these species and other important species are given in Fig. 3 (species nomenclature is defined in the species dictionary in Supplementary material). Also, the validation results for all of the species are provided as Supplementary material.

In the studies by Battin-Leclerc [13] and Meng et al. [11] two different methods, GC and cavity ring-down spectroscopy (CRDS), were used to measure some important intermediate species during 1-hexene oxidation. At 625 K, the mole fractions of formaldehyde measured using CRDS are approximately 50% higher than those measured using the GC method. The CRDS results show that the peak values of formaldehyde mole fraction at 625 K and 850 K are very similar. For *n*-pentanal and hydroxyl cyclic ethers, only the GC method was used in the measurements. The model predicts well all of the species except for $C_6H_{11}$OH1O2–5, which is over-predicted by a factor of three. This can be due to the large uncertainty in the measurement of hydroxyl cyclic ethers. In the study of Battin-Leclerc [13], it was suggested that $C_6H_{11}$OH1O2–5 was the major hydroxyl cyclic ether based on their kinetic insight. However, this species was not detected in the experiments, as this compound may decompose during ionization or it has a very low cross-section. Formaldehyde and *n*-pentanal are the major products formed from the Waddington mechanism. The results for formaldehyde and *n*-pentanal chemistry validations are shown in Fig. S2 of the Supplementary material. Figure 4 shows the flux and sensitivity analyses results for *n*-pentanal at 625 K. Approximately 98% of *n*-pentanal is formed via the Waddington reaction pathways. However, the Waddington reaction pathway only contributes about 10% of total concentration of formaldehyde as it is produced by many pathways. The simulation results indicate that the fuel flux proceeding through the Waddington reaction pathways is correct. However, there are no further experimental results, such as concentration measurements of different hydroxyl cyclic ethers to help validate the branching ratios. In this study, the rate constants calculated by Zádor et al. [16] and a branching ratio of 75:25 of ȮH addition to the terminal and central carbon sites for 1-hexene are used. In this study, the rate constants for ȮH addition to the double bond and H-atom abstraction by ȮH radicals from the allylic carbon site are slightly different to those employed in our previous studies [26,49] with both being decreased here by approximately 40%. These new rate constants mainly affect the JSR predictions in the temperature range 500 – 750 K. The Waddington mechanism was studied previously [19,25]. The isomerization of hydroxy–alkylperoxy radicals forming hydroperoxy-alkoxy radicals were theoretically calculated in both studies [19,25], and the rate constants from the two studies are within a factor of two. In the study of [19], the “non-Waddington” pathways via internal H-atom re-arrangements of H-atoms on other carbon sites to form alcoholic hydroperoxyl-alkyl radicals and $H\dot{O}_2$ elimination are also studied, and these reaction pathways are proven to be important in the low-temperature chemistry of large alkenes [26,49].

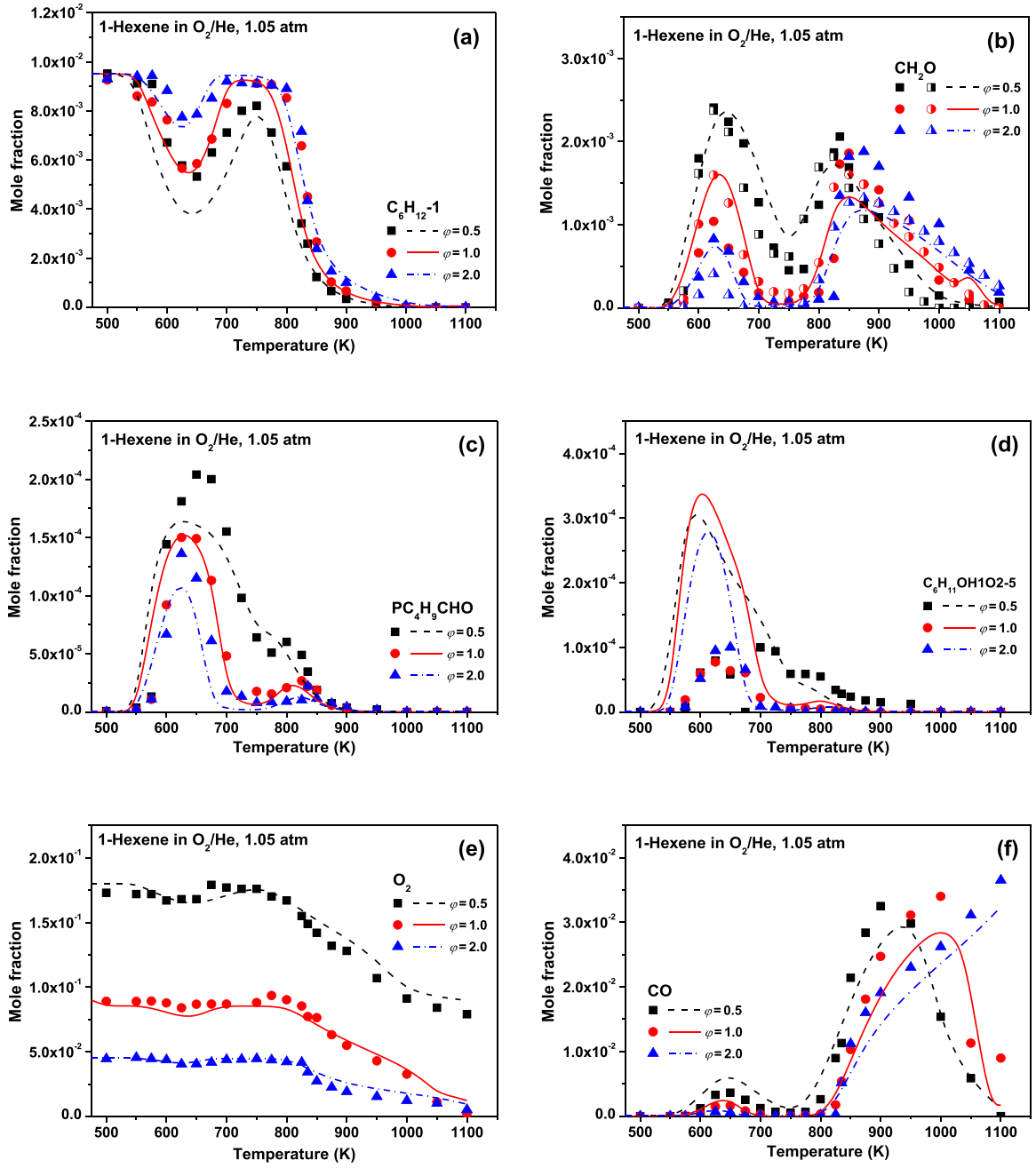


**Fig. 3.** Comparison of experiment and simulation results of 1-hexene JSR data [11]. Solid symbols: experiment data using GC method. Half-filled symbols: experiment data using CRDS method. Solid lines: simulation results with current model. Only validations for important species in the low-temperature chemistry are given here and all of the validation results are provided as Supplementary material.

### 3.2. Hexenyl radical isomerization

The alkenyl radical isomerization reactions are important for linear alkenes with a carbon number larger than four, mainly because the longer carbon chain facilitates isomerization reactions with lower energy barriers. The rate constants calculated by Wang et al. [23] and Sun et al. [24] are used in this study. Both the isomerization between hexenyl radicals and to cyclohexyl radical are included, Eqn. (5).

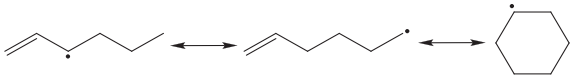

(5)

As shown in Figure 5(a), hexenyl radical isomerization has almost no effect on the reactivity of 1-hexene, except for a slight decrease in reactivity at intermediate temperatures (750 – 800 K). However, the JSR results show that hexenyl radical isomerization does affect the production of cyclohexene, an important intermediate. Without the isomerization included, the simulated mole fraction of cyclohexene in the JSR is negligible for all temperatures investigated. With the isomerization included, Fig. 5(b), the model, including hexenyl radical isomerization, predicts the mole fraction of cyclohexene below 750 K and under-predicts the mole fraction by a factor of three in the intermediate-temperature range.

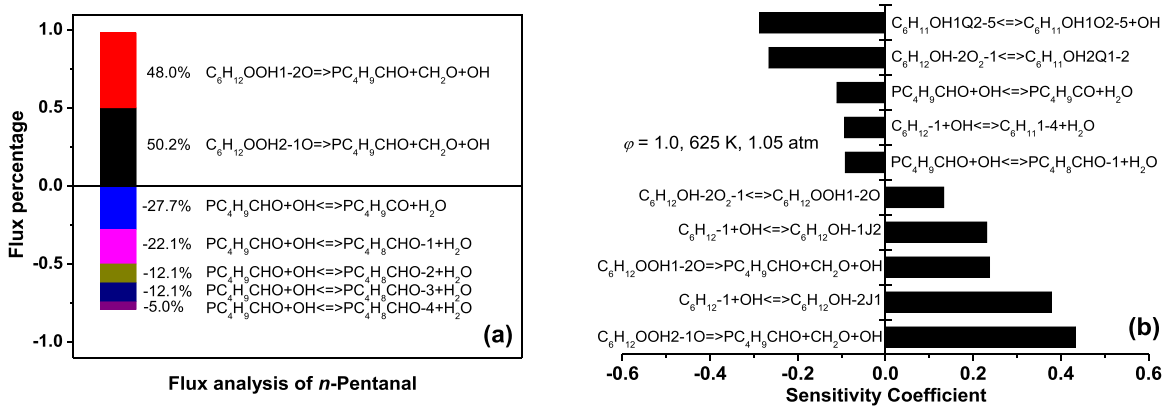


**Fig. 4.** (a) Flux and (b) sensitivity analyses of *n*-pentanal during 1-hexene oxidation in a JSR at 625 K, $\varphi$ = 1.0 and 1.05 atm [11] based on the current model.

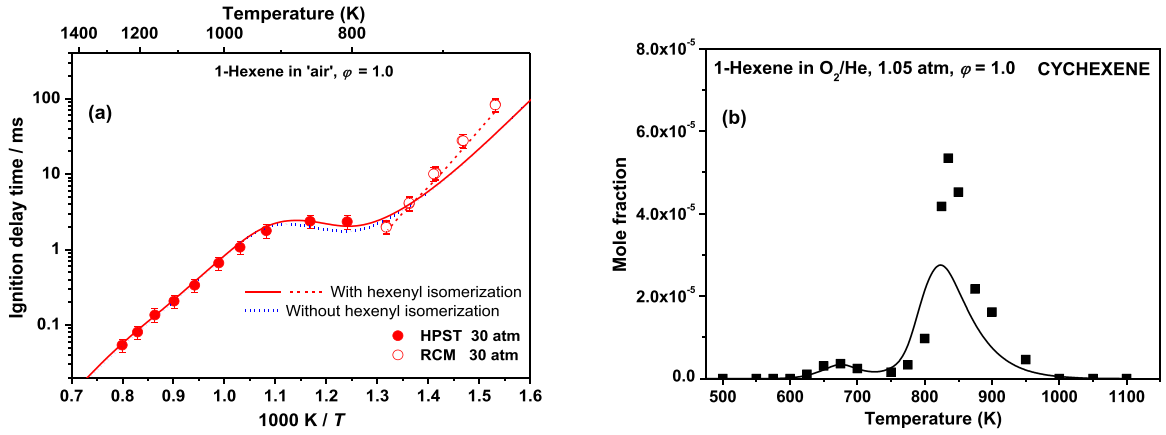


**Fig. 5.** (a) Comparison of simulation results with and without hexenyl radical isomerization. IDTs measured in this study. Solid and dot lines: simulations assuming constant-volume conditions. Dash lines: RCM simulations including the facility effects. (b) Comparisons of model predictions for cyclohexene (including hexenyl radical isomerization) with JSR data for 1-hexene [11].

### 3.3. Alkenyl-peroxy radical ($R\dot{O}_2$) reactions

The reaction pathways of alkenyl-peroxy radicals are important to the low-temperature chemistry of 1-alkenes with a carbon number larger than five [26]. For the current model, the reactions of $H\dot{O}_2$ elimination, isomerizing to $\dot{Q}OOH$ and cycloaddition reactions are included, as shown in Eqns. (6 – 8), and consistent rate constants and thermochemistry with 1-pentene [49] are used. As the longer carbon chain length of 1-hexene compared to 1-pentene decreases the energy barrier of $R\dot{O}_2$ isomerization to $\dot{Q}OOH$, these reaction pathways show larger effects on the low-temperature chemistry of 1-hexene.


(6)

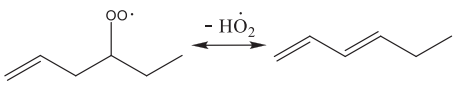


(7)


(8)

## 4. Results and discussions

### 4.1. Model performance against experimental idt data

Figures 6 and 7 show the experiment and simulation IDT results using the current model. As can be seen for these fuel/'air' mixtures, the IDTs of 1-hexene decrease with increasing pressure and equivalence ratios. In the experiments and simulations, NTC behavior is seen for all conditions except for 30 atm and $\varphi$ = 2.0 where the IDTs do not display an actual negative temperature dependence. The experiments show NTC behavior which is consistent with previous RCM experimental results [10], [12]. These previous stoichiometric experiments for 1-hexene reported a slight NTC in IDT at ~ 7.5 atm and a more pronounced NTC behavior at 10 atm. In the RCM experiments, a two-stage ignition behavior is observed at temperatures below 900 K, and both the first-stage and total IDT data are presented in Fig. 6. As shown in Fig. 6, the current model is slightly fast (factor of two) in the low-temperature range at fuel-rich conditions. Both the first-stage and total IDTs at 15 and 30 atm are well predicted. The current model predicts well the auto-ignition behavior of 1-hexene in both the low- and high-temperature regimes. The IDTs measured at diluted and low-pressure conditions from the literature were also simulated with the current model and the results are shown in Fig. S3 and Fig. S4 of the Supplementary material.

Figures 6 and 7 also show the pressure effects and equivalence ratio effects. The reactivity of 1-hexene increases with increasing pressure at all equivalence ratios and increases with increasing

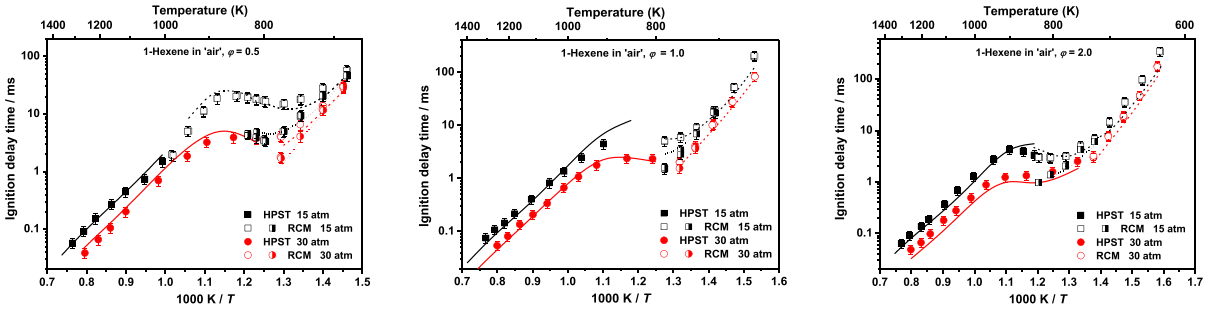


**Fig. 6.** Effects of pressures on 1-hexene IDTs. (a) $\varphi = 0.5$, (b) $\varphi = 1.0$, (c) $\varphi = 2.0$. Solid symbols: HPST IDTs. Half-filled and open symbols represent the first-stage and total RCM IDTs, respectively. Solid lines: simulations assuming constant-volume conditions. Dash lines: RCM simulations including the facility effects. Dotted lines: simulations of RCM first-stage IDTs.

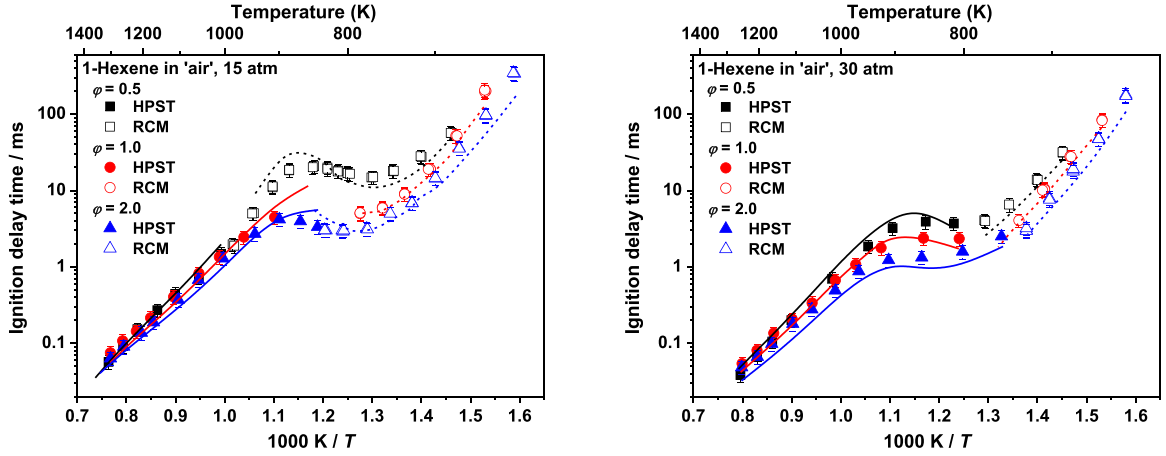


**Fig. 7.** Effects of equivalence ratios on 1-hexene IDTs. (a) 15 atm, (b) 30 atm. Solid symbols: HPST IDTs. Open symbols: RCM IDTs. Solid lines: simulations assuming constant-volume conditions. Dash lines: RCM simulations including the facility effects.

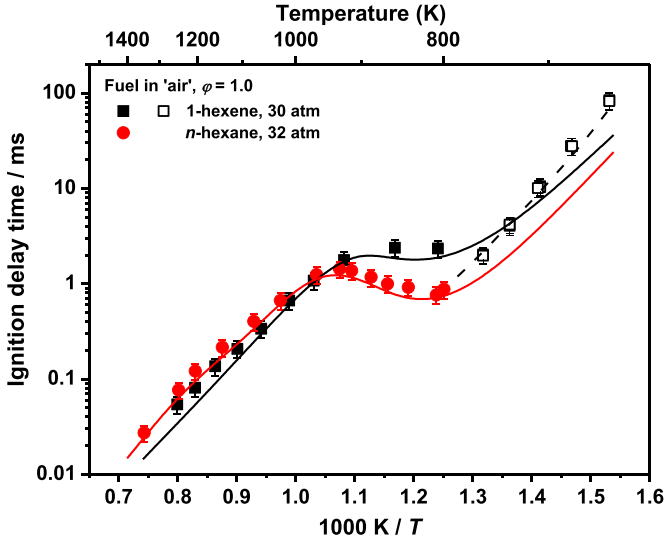


**Fig. 8.** Comparison of fuel reactivity between 1-hexene and *n*-hexane. The *n*-hexane IDTs from [37] are measured for fuel in 'air' at $\varphi = 1.0$ and 32 atm. Solid and open symbols represent HPST and RCM IDTs, respectively. Solid lines: simulations assuming constant-volume conditions. Dash lines: RCM simulations including the facility effects. The simulation results are based on the current mechanism.

equivalence ratios at both pressures, and the current model captures this effect well.

Figure 8 shows a comparison of the fuel reactivity of 1-hexene and *n*-hexane in the temperature range 625 – 1540 K. The *n*-hexane IDTs were taken at a slightly higher pressure (~ 32 atm) than those for 1-hexene (30 atm), and both data sets were measured in the HPST at NUIG. The current model can capture well the IDTs of both fuels. 1-hexene is slower to ignite compared to *n*-hexane at temperatures below 950 K and it shows a less pronounced NTC behavior which is similar to that of 1-pentene and 1-heptene [26]. However, at temperatures above 950 K, 1-hexene is faster to ignite compared to *n*-hexane and the current model can capture this behavior well although the predicted fuel reactivity exceeds that of the experiments above 1100 K. The reason of this relative difference between the two fuels is analyzed in Section 4.3.

### *4.2. Model performance against shock-tube CO and $H_2O$ time histories*

Figures 9 and 10 show the comparison of experimental and simulation results of CO and $H_2O$ time histories at the stoichiometric condition and ~1.4 atm using the current model. Figure 11 shows the overall model performance at different conditions of equivalence ratio and temperature. Only validation results for a few cases at $\varphi = 1.0$ are shown here, with all of the validation results at $\varphi = 0.5$, 1.0 and 2.0 provided in Fig. S5 and Fig. S6 of the Supplementary material. These experimental data were measured at ~1.5 atm and at 99.5% dilution. The current model slightly under-predicts the maximum mole fraction of CO at temperatures above 1600 K. Overall, the current model captures both the timing and the shape of the CO and $H_2O$ time histories at various temperatures. It can also capture the induction time ($\tau_{ind}$) of both CO and $H_2O$, as well as the time-to-peak CO ($\tau_{max}$) and the peak CO

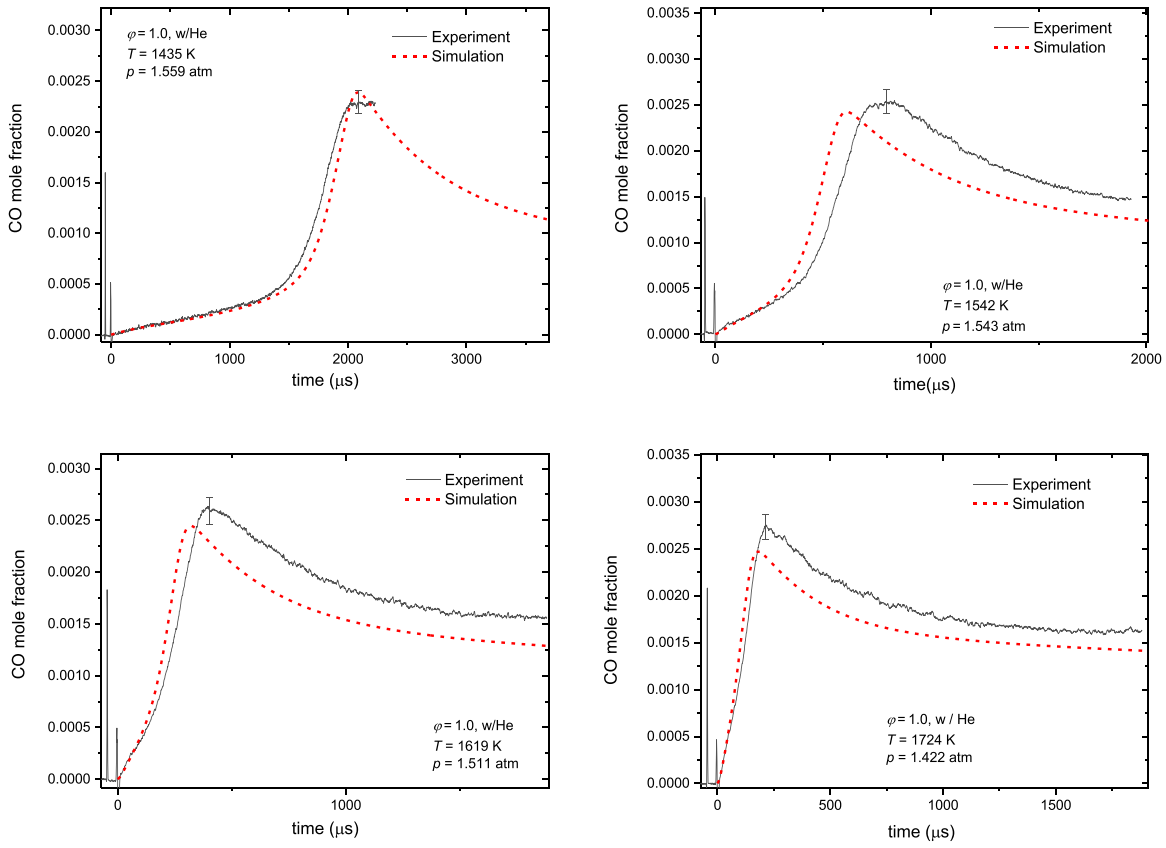


**Fig. 9.** Experiment and simulation results of shock-tube CO time histories at stoichiometric conditions and different temperatures and pressures of 1.4 to 1.5 atm. Solid lines: experiment data. Dash lines: simulation results with current model.

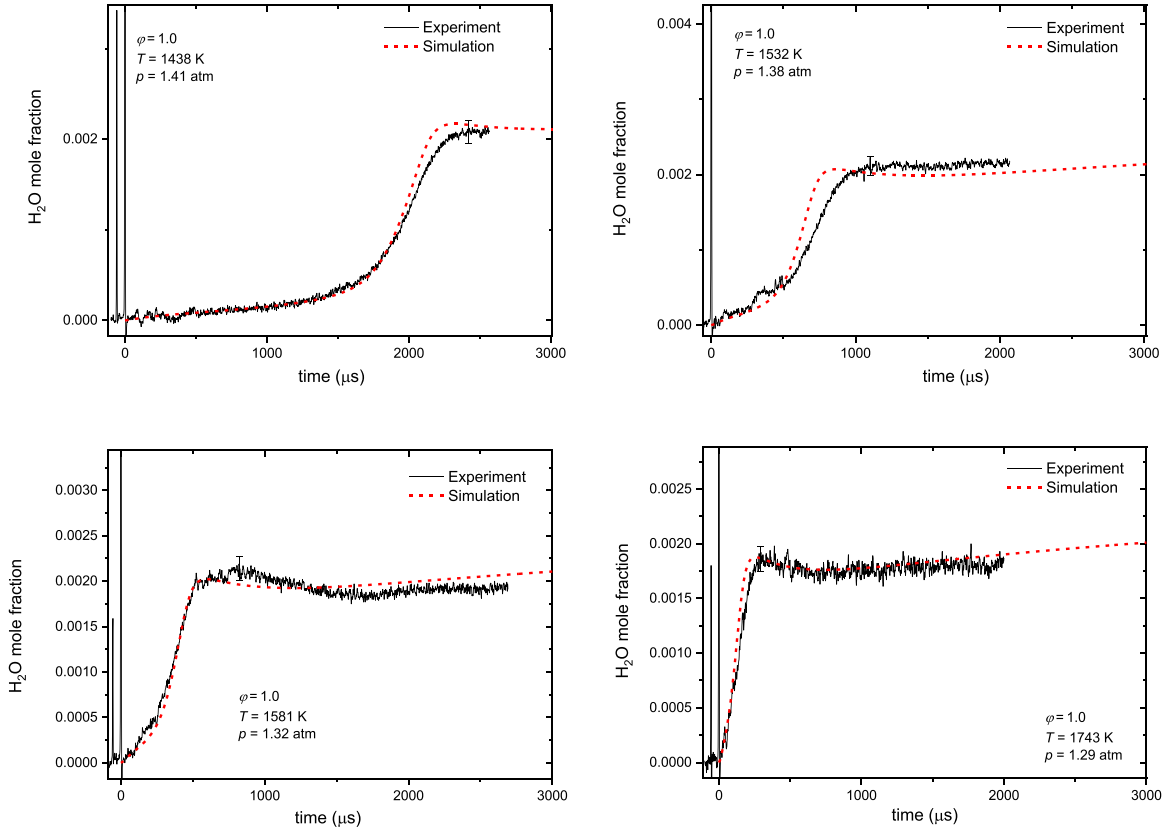


**Fig. 10.** Experiment and simulation results of shock-tube $H_2O$ time histories at stoichiometric conditions and different temperatures and pressures of 1.3 to 1.4 atm. Solid lines: experiment data. Dash lines: simulation results with current model.

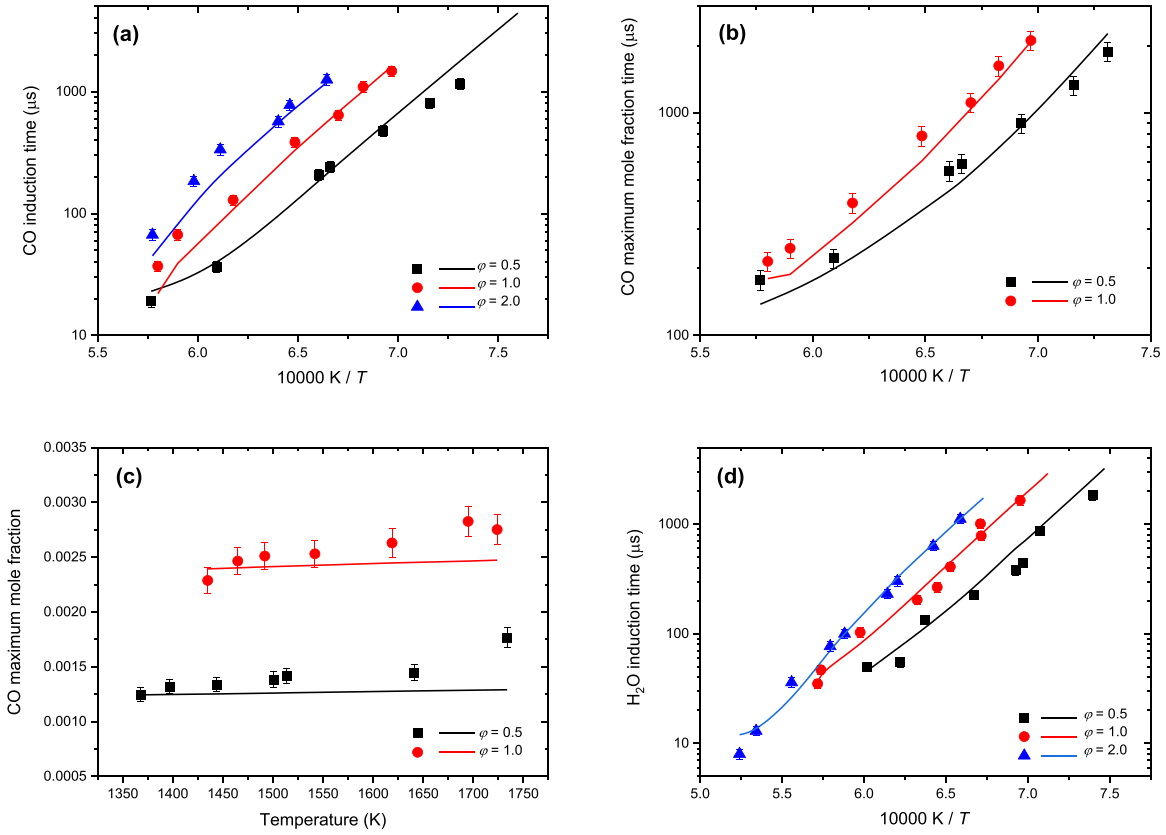


**Fig. 11.** Experimental and simulated results of shock-tube at pressures ~1.4 atm. (a) CO induction time, (b) CO maximum mole fraction time, (c) CO maximum mole fraction, and (d) $H_2O$ induction time. Symbols: experimental results. Solid lines: simulation results.

mole fractions at all conditions investigated, Fig. 11. Both CO and ȮH radical profiles are important indicators of reaction progress and are particularly important in helping capture high-temperature heat release. CO can react with hydroxyl radicals in the reaction CO + ȮH = $CO_2$ + Ḣ, with the Ḣ atoms so produced further reacting with ȮH radicals to form $H_2O$. Both reactions are strongly exothermic and lead to significant heat release prior to fuel autoignition. The current model is in good agreement with the experimental measurements, Figs. 9 and 10, indicating the reliability of the underlying base chemistry.

### 4.3. Flux and sensitivity analyses based on the current model

The Chemkin-PRO [44] software was used to perform flux and sensitivity analyses. Figure 12 shows the flux analysis results for 1-hexene oxidation at different temperatures, with only the major reaction pathways shown.

At 650 K, 95% of 1-hexene is consumed by reacting with ȮH, including abstraction by ȮH (ȮH radical is included in Fig. 12 as the sum of radicals, Ṙ). Approximately 50% of the fuel is consumed by ȮH radical addition to the double bond, whereas 45% is consumed via H-atom abstraction, forming four different hexenyl radicals. As the allylic C–H bond is weakest, the formation of 1-hexen-3-yl ($\dot{C}_6H_{11}$1–3) is the most favored (15.0%). Most of these radicals react with $H\dot{O}_2$ radicals and eventually form $C_6H_{11}\dot{O}$1–3/$C_6H_{11}\dot{O}$2–1 hexenyloxy radicals and ȮH. The $C_6H_{11}\dot{O}$1–3 radicals mainly decompose and produce acrolein and *n*-propyl radicals. All of the other three hexenyl radicals, 1-hexen-4-yl ($\dot{C}_6H_{11}$1–4), 1-hexen-5-yl ($\dot{C}_6H_{11}$1–5) and 1-hexen-6-yl ($\dot{C}_6H_{11}$1–6) mainly add to $O_2$ producing alkenyl-peroxy radicals. For $C_6H_{11}1\dot{O}_2$–4 radicals, one major reaction pathway is via $H\dot{O}_2$ elimination as the allylic C–H bond is the weakest, and the other major reaction pathway is cycloaddition. $C_6H_{11}1\dot{O}_2$–5 and $C_6H_{11}1\dot{O}_2$–6 radicals mainly isomerize to Q̇OOH radicals via six- and seven-membered transition state rings as the allylic C–H bond is the weakest. ȮH radical addition to the terminal and central carbon sites leads to the formation of $\dot{C}_6H_{12}$OH-1j2 and $\dot{C}_6H_{12}$OH-2j1 radicals, respectively. These can add to $O_2$ producing $C_6H_{12}$OH-$1\dot{O}_2$–2 and $C_6H_{12}$OH-$2\dot{O}_2$–1 radicals, followed by internal abstraction of the alkoxy H-atom with subsequent decomposition of the hydroperoxy-alkoxy radical, leading through the Waddington mechanism. The $C_6H_{12}$OH-$1\dot{O}_2$–2 and $C_6H_{12}$OH-$2\dot{O}_2$–1 radicals can also go through a “non-Waddington” pathway via internal H-atom re-arrangements of H-atoms on other carbon sites to form alcoholic hydroperoxyl-alkyl radicals. These radicals can further add to $O_2$ and proceed through chain branching pathways, accounting for 16.0% of the overall fuel flux.

At 800 K, the fraction of ȮH radical addition to the double bond decreases due to the competition with H-atom abstraction by ȮH radicals. Figure 8 shows that 1-hexene presents a less pronounced NTC behavior compared to *n*-hexane, which was discussed in detail previously [26], and only a brief explanation will be given here. The NTC behavior observed in alkanes is due to the competition between chain branching and propagation leading primarily from $R\dot{O}_2$ and Q̇OOH radicals, with chain branching producing two reactive ȮH radicals and a carbonyl-alkoxy radical. Chain propagation produces: 1) less reactive $H\dot{O}_2$ radicals and an olefin, 2) cyclic ethers and ȮH radicals, and 3) a smaller alkyl radical via $\beta$-scission. With increasing temperature in the NTC region, the fuel flux to chain branching decreases while the flux to chain propagation increases, which leads to NTC behavior. For 1-hexene, the chain propagation reaction pathways (Waddington mechanism and $\dot{C}_6H_{11}$1–3 reaction with $H\dot{O}_2$) produce reactive ȮH rather than $H\dot{O}_2$ radicals. The competition of chain propagation and chain branching pathways shows a relatively smaller effect on auto-ignition for

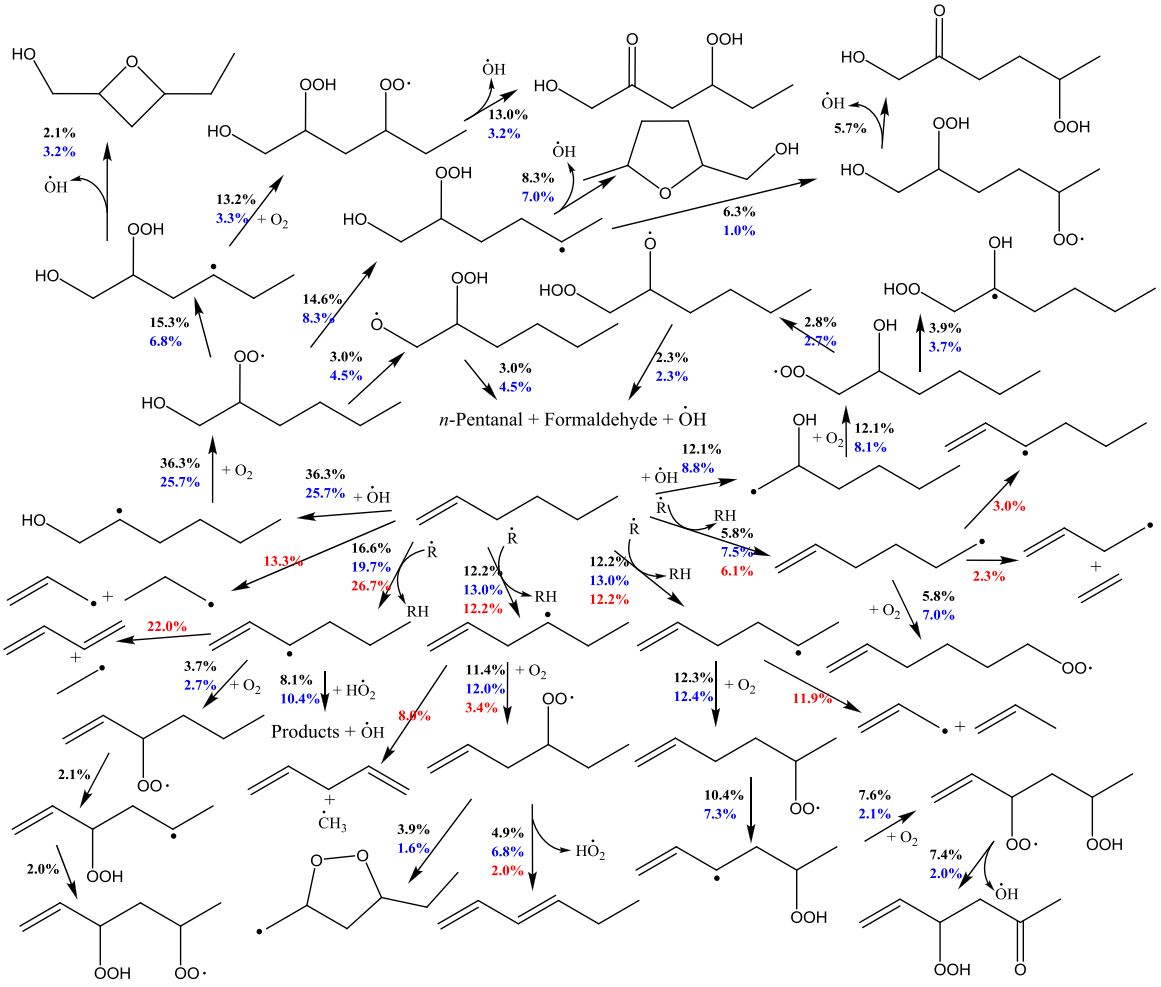


**Fig. 12.** Flux analyses for 1-hexene at $\varphi = 1.0$ in 'air', 30 atm and 20% fuel consumption. Numbers represent the percentage of fuel flux that goes into a particular species. Black numbers: 650 K. Blue numbers: 800 K. Red numbers: 1200 K. Ṙ is the sum of ȮH, $H\dot{O}_2$ and $\dot{C}H_3$ radicals and Ḣ and Ö atoms.

alkenes compared to alkanes. Therefore, 1-hexene presents a less pronounced NTC behavior compared to *n*-hexane.

At 1200 K, 1-hexene is mostly consumed via H-atom abstraction (58.4%), with ȮH radicals contributing most (35.8%), producing alkenyl radicals. 1-Hexene is also consumed via unimolecular decomposition reactions (13.3%), while the Waddington mechanism is negligible at 1200 K. Most of the $\dot{C}_6H_{11}$1–3 and $\dot{C}_6H_{11}$1–5 radicals produced in these processes undergo $\beta$-scission reactions. For $\dot{C}_6H_{11}$1–4 radicals, a large proportion (~60%) undergo $\beta$-scission producing 1,4-pentadiene and methyl radicals. Approximately 27% of $\dot{C}_6H_{11}$1–4 radicals add to $O_2$ producing alkenyl-peroxyl radicals, and subsequently undergo $H\dot{O}_2$ elimination producing 1,3-hexadiene and $H\dot{O}_2$ radicals. Another important reaction pathway is H-atom addition to the double bond which ultimately produces a smaller alkene and an alkyl radical.

Figure 8 shows that at 1200 K 1-hexene presents a higher reactivity compared to *n*-hexane. Flux analysis for *n*-hexane at the same conditions were performed and the results are provided in Fig. S7. For *n*-hexane oxidation, more than 70% of fuel radicals undergo $\beta$-scission forming smaller alkenes and alkyl radicals. About 30% of *n*-hexane leads to the formation of propene, which is the major reaction pathway. For 1-hexene, about 22% of the fuel flux is consumed producing 1,3-butadiene and ethyl radicals, and only 12% of the fuel is consumed producing propene. In our previous study [26], the fuel reactivities of 1-alkene fuels are compared directly based on IDT measurement results. At high temperatures (> 950 K), propene and isobutene present significantly lower reactivity compared to other 1-alkenes. Therefore, as *n*-hexane produces more propene compared to 1-hexene, this contributes to a lower reactivity of *n*-hexane compared to 1-hexene at high temperatures.

Figure 13 presents the brute force sensitivity analysis results for 1-hexene. Positive values indicate reactions that inhibit reactivity and negative values promote reactivity. At 650 K and 30 atm in the low temperature range in Fig 13(a), the reactions which promote reactivity include ȮH addition to the double bond and the following chain branching reactions, which is consistent with the flux analysis results. The most sensitive promoting reaction is the ȮH addition to the terminal carbon of the 1-hexene double bond. This reaction eventually leads to chain branching through the decomposition of a hydroxyl ketohydroperoxide ($C_6H_{11}$OH1KET2–4) which is the third most promoting reaction. At 800 K and 30 atm in the NTC region, isomerization of hexenyl-peroxy radicals promote reactivity due to the chain branching reaction pathways. This sequence is seen in Fig. 13(b) in several promoting reactions. First, H-atom abstraction by ȮH from the allylic C–H site produces an allylic radical ($\dot{C}_6H_{11}$1–3) which is the second most promoting reaction. Thereafter, $\dot{C}_6H_{11}$1–3 radicals add to $O_2$, producing alkenyl-peroxy ($C_6H_{11}1\dot{O}_2$–3) radicals which mostly isomerize to $\dot{C}_6H_{10}$OOH3–5 radicals in the fourth most promoting reaction. Finally, $\dot{C}_6H_{10}$OOH3–5 radicals undergo a second addition to $O_2$, producing $C_6H_{10}$OOH3–5$\dot{O}_2$ radicals which is the most promot-

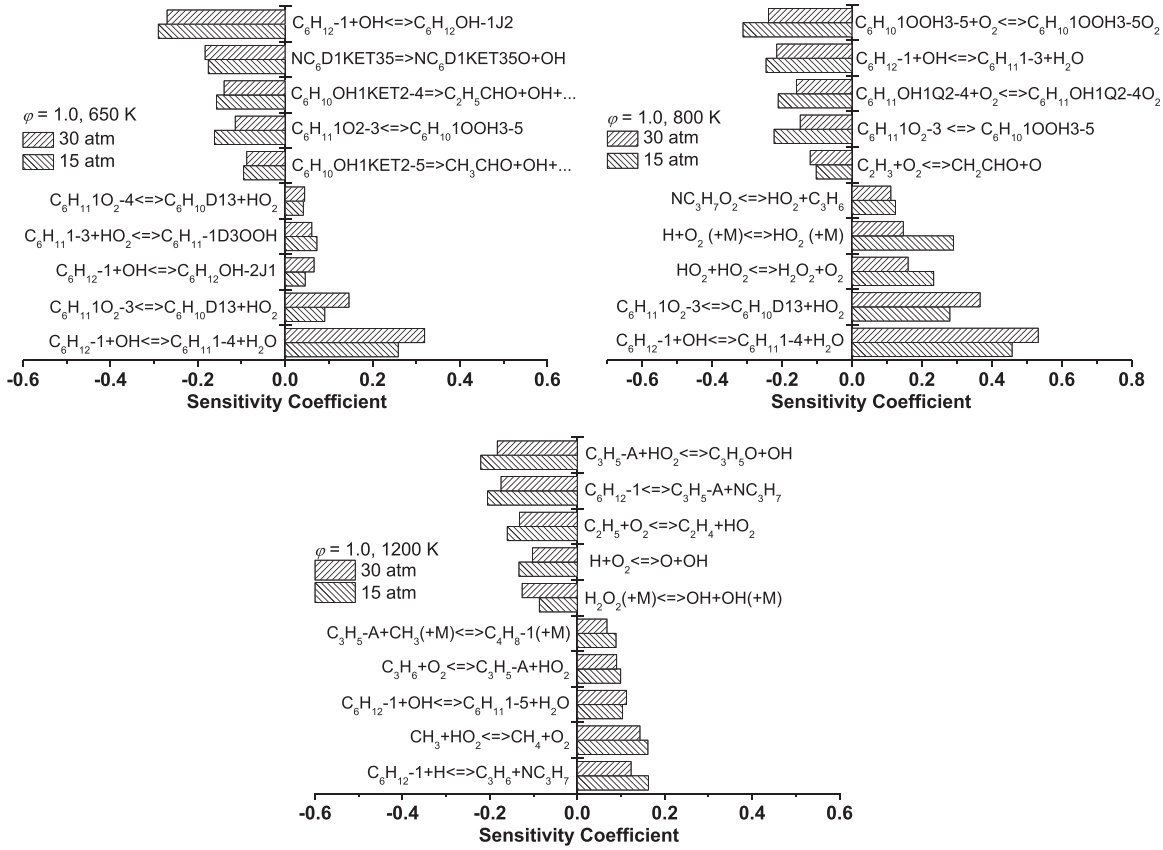


**Fig. 13.** Sensitivity analyses for 1-hexene at $\varphi = 1.0$ in 'air', $p = 15$ and 30 atm. (a) $T = 650$ K, (b) $T = 800$ K, and (c) $T = 1200$ K.

ing reaction and leads to chain branching. At 650 and 800 K in Fig. 13(a) and (b), the most inhibiting reaction is H-atom abstraction from 1-hexene by ȮH at an alkyl site, producing $\dot{C}_6H_{11}$1–4 radicals. $\dot{C}_6H_{11}$1–4 radicals mainly add to $O_2$ producing $\dot{C}_6H_{11}1O_2$–4 radicals, followed by $H\dot{O}_2$ elimination, as the allylic C–H bond is weak. This reaction competes with the promoting reaction pathways of ȮH addition and for ȮH abstraction at the allylic site discussed above. At 1200 K, in the high-temperature regime illustrated in Fig. 13(c), the overall magnitude of the sensitivity coefficients drops compared to the NTC and low temperature regions. At 1200 K, decomposition of the fuel to an allyl ($C_3H_5$-a) and an *n*-propyl ($n\dot{C}_3H_7$) radical is the second most important reaction promoting reactivity. The subsequent reaction of an allyl raidcal with an $H\dot{O}_2$ radical to form a reactive ȮH radical is the most promoting reaction.

## 5. Conclusions

In this study, various experimental data for 1-hexene oxidation were measured in different facilities. IDTs of 1-hexene at equivalence ratios of 0.5, 1.0 and 2.0 in 'air', at 15 and 30 atm and over a wide temperature range (600 – 1300 K) were measured using both a HPST and an RCM, and both the first-stage and total IDT data were recorded. Also, CO and $H_2O$ time histories for 1-hexene oxidation were measured around 1.5 atm under highly diluted conditions.

A new kinetic model was developed and validated against the newly taken experimental data as well as experimental data from the literature. Based on the validation results of the JSR species profiles, the rate constants and branching ratio of ȮH addition to the terminal and central carbon sites for 1-hexene were validated.

The current model can predict well the auto-ignition behavior of 1-hexene. Flux and sensitivity analyses show that the reactions associated with hydroxy radical addition to the double bond contributes most to the low-temperature reactivity of 1-hexene. In the NTC region, the isomerization of hexenyl-peroxy promotes fuel reactivity due to its associated chain branching pathways. In the high temperature region, the decomposition of 1-hexene to allyl radicals, which subsequently reacts with $H\dot{O}_2$ radicals, promotes reactivity.

## Declaration of Competing Interest

The authors declare that they have no known competing financial interests or personal relationships that could have appeared to influence the work reported in this paper.

## Acknowledgments

The authors at NUI Galway recognize funding support from Science Foundation Ireland (SFI) through project number 16/SP/3829 and also funding from Computational Chemistry LLC. The work at LLNL was performed under the auspices of the U.S. Department of Energy (DOE) by Lawrence Livermore National Laboratory under Contract DE-AC52-07NA27344 and was conducted as part of the Co-Optimization of Fuels and Engines (Co-Optima) project sponsored by the DOE Office of Energy Efficiency and Renewable Energy (EERE), Bioenergy Technologies and Vehicle Technologies Offices. The efforts at Texas A&M University (TAMU) and Stephen F. Austin State University were supported primarily by the TEES Turbomachinery Laboratory. The help of Dr. Clayton Mulvihill (TAMU) in the interpretation of the laser absorption experiments is acknowledged.

## Supplementary materials

Supplementary material associated with this article can be found, in the online version, at doi:10.1016/j.combustflame.2021.111516.

## References


[1] G. Vanhove, G. Petit, R. Minetti, Experimental study of the kinetic interactions in the low-temperature autoignition of hydrocarbon binary mixtures and a surrogate fuel, Combust. Flame 145 (3) (2006) 521–532.
[2] M. Yahyaoui, N. Djebaïli-Chaumeix, P. Dagaut, C.E. Paillard, S. Gail, Experimental and modelling study of gasoline surrogate mixtures oxidation in jet stirred reactor and shock tube, Proc. Combust. Inst. 31 (1) (2007) 385–391.
[3] M. Mehl, W.J. Pitz, C.K. Westbrook, H.J. Curran, Kinetic modeling of gasoline surrogate components and mixtures under engine conditions, Proc. Combust. Inst. 33 (2011) 193–200.
[4] S.M. Sarathy, A. Farooq, G.T. Kalghatgi, Recent progress in gasoline surrogate fuels, Prog. Energy Combust. Sci. 65 (2018) 67–108.
[5] S. Yang, Q. Wang, H.J. Curran, M. Jia, Development of a 5-component gasoline surrogate model using recent advancements in the detailed H2/O2/CO/C1-C3 mechanism for decoupling methodology, Fuel 283 (2021) 118793.
[6] H. Yuan, Z. Chen, Z. Zhou, Y. Yang, M.J. Brear, J.E. Anderson, Formulating gasoline surrogate for emulating octane blending properties with ethanol, Fuel 261 (2020) 116243.
[7] L.R. Cancino, A. da Silva, A.R. De Toni, M. Fikri, A.A.M. Oliveira, C. Schulz, H.J. Curran, A six-compound, high performance gasoline surrogate for internal combustion engines: experimental and numerical study of autoignition using high-pressure shock tubes, Fuel 261 (2020) 116439.
[8] S. Touchard, R. Fournet, P.A. Glaude, V. Warth, F. Battin-Leclerc, G. Vanhove, M. Ribaucour, R. Minetti, Modeling of the oxidation of large alkenes at low temperature, Proc. Combust. Inst. 30 (2005) 1073–1081.
[9] M. Yahyaoui, N. Djebaïli-Chaumeix, C.-.E. Paillard, S. Touchard, R. Fournet, P.A. Glaude, F. Battin-Leclerc, Experimental and modeling study of 1-hexene oxidation behind reflected shock waves, Proc. Combust. Inst. 30 (2005) 1137–1145.
[10] M. Mehl, G. Vanhove, W.J. Pitz, E. Ranzi, Oxidation and combustion of the n-hexene isomers: a wide range kinetic modeling study, Combust. Flame. 155 (2008) 756–772.
[11] X. Meng, A. Rodriguez, O. Herbinet, T. Wang, F. Battin-Leclerc, Revisiting 1-hexene low-temperature oxidation, Combust. Flame. 181 (2017) 283–299.
[12] M. Mehl, W.J. Pitz, C.K. Westbrook, K. Yasunaga, C. Conroy, H.J. Curran, Autoignition behavior of unsaturated hydrocarbons in the low and high temperature regions, Proc. Combust. Inst. 33 (2011) 201–208.
[13] F. Battin-Leclerc, A. Rodriguez, B. Husson, O. Herbinet, P.A. Glaude, Z. Wang, Z. Cheng, F. Qi, Products from the oxidation of linear isomers of hexene, J. Phys. Chem. A. 118 (2014) 673–683.
[14] M. Yahyaoui, N. Djebaïli-Chaumeix, P. Dagaut, C.-.E. Paillard, S. Gail, Kinetics of 1-hexene oxidation in a JSR and a shock tube: experimental and modeling study, Combust. Flame 147 (1–2) (2006) 67–78.
[15] G. Vanhove, M. Ribaucour, R. Minetti, On the influence of the position of the double bond on the low-temperature chemistry of hexenes, Proc. Combust. Inst. 30 (2005) 1065–1072.
[16] J. Zádor, A.W. Jasper, J.A. Miller, The reaction between propene and hydroxyl, Phys. Chem. Chem. Phys. 11 (2009) 11040–11053.
[17] J. Zádor, S.J. Klippenstein, J.A. Miller, Pressure-dependent OH yields in alkene + $HO_2$ reactions: a theoretical study, J. Phys. Chem. A. 115 (2011) 10218–10225.
[18] X. You, Y. Chi, T. He, Theoretical analysis of the effect of C=C double bonds on the low-temperature reactivity of alkenylperoxy radicals, J. Phys. Chem. A. 120 (2016) 5969–5978.
[19] J.C. Lizardo-Huerta, B. Sirjean, R. Bounaceur, R. Fournet, Intramolecular effects on the kinetics of unimolecular reactions of $\beta$-HOROO and HOQOOH radicals, Phys. Chem. Chem. Phys. 18 (2016) 12231–12251.
[20] X. Sun, W. Zong, J. Wang, Z. Li, X. Li, Pressure-dependent rate rules for cycloaddition, intramolecular H-shift, and concerted elimination reactions of alkenyl peroxy radicals at low temperature, Phys. Chem. Chem. Phys. 21 (20) (2019) 10693–10705.
[21] S.S. Vasu, L.K. Huynh, D.F. Davidson, R.K. Hanson, D.M. Golden, Reactions of ȮH with butene isomers: measurements of the overall rates and a theoretical study, J. Phys. Chem. A. 115 (2011) 2549–2556.
[22] C.W. Zhou, J.M. Simmie, K.P. Somers, C.F. Goldsmith, H.J. Curran, Chemical Kinetics of Hydrogen Atom Abstraction from Allylic Sites by $^3O_2$; Implications for Combustion Modeling and Simulation, J. Phys. Chem. A. 121 (2017) 1890–1899.
[23] K. Wang, S.M. Villano, A.M. Dean, The impact of resonance stabilization on the intramolecular hydrogen-atom shift reactions of hydrocarbon radicals, Chem. Phys. Chem. 16 (2015) 2635–2645.
[24] Y. Sun, C.W. Zhou, K.P. Somers, H.J. Curran, Ab initio/transition-state theory study of the reactions of Ċ5H9 species of relevance to 1,3-pentadiene, part I: potential energy surfaces, thermochemistry, and high-pressure limiting rate Constants, J. Phys. Chem. A. 123 (2019) 9019–9052.
[25] Y. Li, Q. Zhao, Y. Zhang, Z. Huang, S.M. Sarathy, A systematic theoretical kinetics analysis for the waddington mechanism in the low-temperature oxidation of butene and butanol isomers, J. Phys. Chem. A. 124 (2020) 5646–5656.
[26] S. Dong, K. Zhang, P.K. Senecal, G. Kukkadapu, S.W. Wagnon, S. Barrett, N. Lokachari, S. Panigaphy, W.J. Pitz, H.J. Curran, A comparative reactivity study of 1-alkene fuels from ethylene to 1-heptene, Proc. Combust. Inst. 38 (2021) 611–619 000.
[27] D. Darcy, C.J. Tobin, K. Yasunaga, J.M. Simmie, J. Würmel, W.K. Metcalfe, T. Niass, S.S. Ahmed, C.K. Westbrook, H.J. Curran, A high pressure shock tube study of n-propylbenzene oxidation and its comparison with n-butylbenzene, Combust. Flame. 159 (2012) 2219–2232.
[28] D. Darcy, H. Nakamura, C.J. Tobin, M. Mehl, W.K. Metcalfe, W.J. Pitz, C.K. Westbrook, H.J. Curran, A high-pressure rapid compression machine study of n-propylbenzene ignition, Combust. Flame. 161 (2014) 65–74.
[29] C. Morley, GasEq, Version 0.76. http://www.gaseq.co.uk, 2004.
[30] Y. Li, C.W. Zhou, H.J. Curran, An extensive experimental and modeling study of 1-butene oxidation, Combust. Flame. 181 (2017) 198–213.
[31] C.J. Aul, W.K. Metcalfe, S.M. Burke, H.J. Curran, E.L. Petersen, Ignition and kinetic modeling of methane and ethane fuel blends with oxygen: a design of experiments approach, Combust. Flame. 160 (2013) 1153–1167.
[32] O. Mathieu, C.R. Mulvihill, E.L. Petersen, Assessment of modern detailed kinetics mechanisms to predict CO formation from methane combustion using shock-tube laser-absorption measurements, Fuel 236 (2019) 1164–1180.
[33] O. Mathieu, C. Mulvihill, E.L. Petersen, Shock-tube water time-histories and ignition delay time measurements for H2S near atmospheric pressure, Proc. Combust. Inst. 36 (2017) 4019–4027.
[34] S.A. Alturaifi, C.R. Mulvihill, O. Mathieu, E.L. Petersen, Speciation measurements in shock tubes for validation of complex chemical kinetics mechanisms: application to 2-Methyl-2-Butene oxidation, Combust. Flame. 225 (2021) 196–213.
[35] O. Mathieu, S.P. Cooper, S. Alturaifi, C.R. Mulvihill, T.M. Atherley, E.L. Petersen, Shock-tube laser absorption measurements of CO and $H_2O$ during iso-octane combustion, Energy Fuels 34 (2020) 7533–7544.
[36] C.R. Mulvihill, O. Mathieu, E.L. Petersen, The unimportance of the reaction $H_2 + N_2O \leftrightarrows H_2O + N_2$: a shock-tube study using $H_2O$ time histories and ignition delay times, Combust. Flame. 196 (2018) 478–486.
[37] K. Zhang, C. Banyon, C. Togbé, P. Dagaut, J. Bugler, H.J. Curran, An experimental and kinetic modeling study of n-hexane oxidation, Combust. Flame. 162 (2015) 4194–4207.
[38] G. Kukkadapu, K. Kumar, C.J. Sung, M. Mehl, W.J. Pitz, Autoignition of gasoline and its surrogates in a rapid compression machine, Proc. Combust. Inst. 34 (2013) 345–352.
[39] E.R. Ritter, J.W. Bozzelli, THERM: thermodynamic property estimation for gas phase radicals and molecules, Int. J. Chem. Kinet. 23 (1991) 767–778.
[40] S.M. Burke, J.M. Simmie, H.J. Curran, Critical evaluation of thermochemical properties of $C_1$–$C_4$ species: updated group-contributions to estimate thermochemical properties, J. Phys. Chem. Ref. Data 44 (2015) 013101.
[41] Y. Li, H.J. Curran, Extensive theoretical study of the thermochemical properties of unsaturated hydrocarbons and allylic and super-allylic radicals: the development and optimization of group additivity values, J. Phys. Chem. A. 122 (2018) 4736–4749.
[42] A. Miyoshi, Molecular size dependent falloff rate constants for the recombination reactions of alkyl radicals with O2 and implications for simplified kinetics of alkylperoxy radicals, Int. J. Chem. Kinet. 44 (2012) 59–74.
[43] R. Sivaramakrishnan, J.V. Michael, Rate constants for OH with selected large alkanes: shock-tube measurements and an improved group scheme, J. Phys. Chem. A. 113 (2009) 5047–5060.
[44] CHEMKIN-PRO 15101Reaction Design, San Diego, 2010.
[45] J. Zádor, J.A. Miller, Unimolecular dissociation of hydroxypropyl and propoxy radicals, Proc. Combust. Inst. 34 (2013) 519–526.
[46] I.O. Antonov, J. Kwok, J. Zádor, L. Sheps, A combined experimental and theoretical study of the reaction OH + 2-butene in the 400–800K temperature range, J. Phys. Chem. A. 119 (2015) 7742–7752.
[47] J.C. Loison, J. Daranlot, A. Bergeat, F. Caralp, R. Mereau, K.M. Hickson, Gas-phase kinetics of hydroxyl radical reactions with $C_3H_6$ and $C_4H_8$: product branching ratios and OH addition site-specificity, J. Phys. Chem. A. 114 (2010) 13326–13336.
[48] E.J. Feltham, M.J. Almond, G. Marston, K.S. Wiltshire, N. Goldberg, Reactions of hydroxyl radicals with alkenes in low-temperature matrices, Spectrochim. Acta - Part A Mol. Biomol. Spectrosc. 56 (2000) 2589–2603.
[49] S. Dong, K. Zhang, E.M. Ninnemann, A. Najjar, G. Kukkadapu, J. Baker, F. Arafin, Z. Wang, W.J. Pitz, S.S. Vasu, S.M. Sarathy, P.K. Senecal, H.J. Curran, A comprehensive experimental and kinetic modeling study of 1- and 2-pentene, Combust. Flame 223 (2021) 166–180.